Soil Dynamics and Earthquake Engineering 104 (2018) 106–116

Contents lists available at ScienceDirect

Soil Dynamics and Earthquake Engineering

journal homepage: www.elsevier.com/locate/soildyn

Site amplifications and the effect on local magnitude determination at stations of the surface–downhole network in Taiwan

Chun-Hsiang Kuo[a,*], Kuo-Liang Wen[b], Che-Min Lin[a], Nai-Chi Hsiao[c], Da-Yi Chen[c]

[a] National Center for Research on Earthquake Engineering, NARL, Taipei, Taiwan
[b] Department of Earth Sciences, National Central University, Chungli, Taiwan
[c] Central Weather Bureau, Taipei, Taiwan

ARTICLE INFO

Keywords:
Site amplification
Downhole
Local magnitude
HHSR
HVSR

ABSTRACT

This study analyzed site effects including PGA and empirical transfer functions at 15 selected surface–downhole stations by using ground motion recordings of earthquakes with $M_L > 4$ during 2012 and 2013 in Taiwan. In addition, we used all strong motion recordings of four large earthquakes ($M_L > 6$) to generate intensity distribution maps and assess the differences in magnitude at the surface and downhole. The site amplification factors of the PGA were calculated using the ratio between the surface and downhole recordings. The mean PGA amplification factors ranged from 2 to an exaggerated value of 20 at different stations. In addition, the power law relationships between the PGAs at the surface and downhole were evaluated to understand how amplification varies as PGA increases. Strong ground motions with and without site effects throughout Taiwan could be observed by comparing intensity distribution maps generated using the surface and downhole accelerations from four large earthquakes with magnitudes > 6. Empirical transfer functions derived using the single-station and two-station methods at the same stations showed comparable dominant frequencies and amplification factors; however, the empirical transfer function derived using the two-station method showed clearer resonance peaks, not only at fundamental frequencies but also at higher mode resonance frequencies. The HHSR and the HVSR were highly similar, particularly at medium frequencies. This finding indicates that the HVSR can be used instead of the HHSR when only the surface recording is available. Moreover, the local magnitudes calculated using surface recordings were higher than those calculated using downhole recordings. The differences are attributed to the amplification caused by the sedimentary layers and resultant in 0.36, 0.46 and 0.49 on average for events with M_L of > 6, 5–6, and 4–5. Furthermore, HHSRs at 5–10 Hz and 1.1–1.7 Hz were strongly correlated with PGA amplifications and M_L differences, respectively.

1. Introduction

The site effect is an important characteristic caused by local unconsolidated sediments and usually results in significant enlargement of the amplitudes and durations of seismic waves. Although their source and path conditions are similar, two adjacent stations may experience a large difference in seismic amplifications when their geological conditions are different [1,2]. Typical cases of site amplifications for strong motions in Taiwan were observed inside the Taipei Basin during the 1986 and 2002 Hualien offshore earthquakes and the 1999 Chi-Chi earthquake. During these large earthquakes, the soft sediments covering the bedrock inside the basin caused significant amplification of the seismic waves, which in turn caused significant damage to buildings, despite the epicentral distances to the Taipei Basin exceeding 90 km.

The two-station [3] and single-station [4] methods are the most widely used approaches for analyzing seismic site effects. The two-station method is widely used to estimate site amplification factors and the horizontal-to-horizontal spectral ratio (HHSR), particularly for seismic design codes [5,6]. This approach requires the identification of an adequate reference site, usually a hard rock site without site effects, for estimating site amplification factors; however, such a site is usually difficult to identify in practice. The single-station method calculates the horizontal-to-vertical spectral ratio (HVSR) to assess the site effect and to obtain a result comparable with that of the two-station method [7]. The simple HVSR method has therefore become extensively applied in site effect studies [2,8,9].

The Taiwan Strong Motion Instrumentation Program (TSMIP) is a national high-density strong ground motion network that has been operating in Taiwan since 1992 [10], with more than 700 stations

* Correspondence to: 200, Sec. 3, Xinhai Rd. Taipei 10668, Taiwan
E-mail address: chkuo@ncree.narl.org.tw (C.-H. Kuo).

http://dx.doi.org/10.1016/j.soildyn.2017.10.003
Received 14 March 2017; Received in revised form 18 September 2017; Accepted 1 October 2017

installed currently. In recent years, the seismic site conditions of more than half of the free-field TSMIP stations have been investigated [11,12]. These data have been used for both local [13–16] and global [17,18] strong motion and site effect studies and for the seismic design code in Taiwan [19]. More detailed site characterizations for TSMIP stations are underway [20–22].

Several downhole seismic arrays have also been installed in Taiwan. In 1985–1991, the Lotung Large-Scale Seismic Test (LLSST) project was conducted by the Taiwan Power Company (TaiPower) and the US Electric Power Research Institute to install free-surface downhole arrays and structural accelerometers in Lotung Town, Ilan. Two downhole arrays consisting of four downhole accelerometers were installed at depths of 6, 11, 17, and 46 m. Subsequently, the Hualien Large-Scale Seismic Test (HLSST) project was conducted to construct a free-surface downhole array and to deploy structural accelerometers in Hualien City for recording near-field strong motions. A total of 12 downhole accelerometers were deployed in 3 downhole arrays at depths of 5, 16, 26, and 53 m. The LLSST and HLSST arrays were a part of the Strong Motion Array in Taiwan project as phase 1 (SMART1) and phase 2 (SMART2), respectively. The two networks played an important role in early strong ground motion monitoring and studies in Taiwan from the 1980s to 1990s [23–25].

To understand the influence of sedimentary layers on the propagation of seismic waves inside the Taipei Basin, the Central Geological Survey and Academia Sinica Institute of Earth Sciences successively deployed 12 strong motion downhole arrays inside the basin, starting in 1991. Currently, eight of these arrays still monitor strong motion. Three to five accelerometers were installed in each array at the surface and at different depths. The obtained strong motion recordings have been used by several studies evaluating site effects and soil nonlinearity in the Taipei Basin [26,27]. In addition, since 2005, seven broadband downhole seismic arrays have been constructed inside the Taipei Basin to monitor microearthquakes. Each array consists of two broadband sensors installed at different depths.

The 1999 Chi-Chi earthquake resulted in damage to the Taichung Harbor area, because of liquefaction caused by strong motion. The Center of Harbor and Marine Technology set up seismographers and piezometers at different depths to monitor seismic waves and pore water pressures in several harbor areas [28]. These downhole arrays can facilitate the understanding of the local site effects in Taiwan, particularly in the Taipei Basin. The downhole seismic arrays introduced above were plotted in Fig. 1 to show their locations.

After the 1995 Hyogoken-Nanbu (Kobe) earthquake in Japan, the National Research Institute for Earth Science and Disaster Prevention installed two nationwide strong motion seismograph networks, the Kyoshin Network (K-NET) and the Kiban Kyoshin Network (KiK-net), to uniformly monitor strong motion throughout Japan [29]. The K-NET is a free-field strong motion network, whereas the KiK-net is an uphole–downhole observation network. Each KiK-net station consists of a strong motion seismograph at the surface and a strong motion seismograph together with a high-sensitivity velocity seismograph (Hi-net) at the bottom of the observation boreholes. The uphole–downhole strong motion stations in Japan (KiK-net) provide useful data for site effect studies [30–32].

To improve earthquake monitoring, earthquake location determination, and early warning capabilities, the Central Weather Bureau (CWB) of Taiwan continues to upgrade seismographs and to construct a national network of surface–downhole stations for the whole of Taiwan. A total of 70 surface–downhole stations are expected to be installed under this project. Twenty-eight stations had been installed by 2013. Wang *et al.* [33] used these data to estimate the attenuation and velocities at the 28 stations. Lai *et al.* [34] studied the spectral decay parameter kappa (κ) in Taiwan by using borehole array data.

To evaluate site effects, this study analyzed the site amplifications of peak ground acceleration (PGA), empirical transfer functions, and the variations of local magnitudes by using the strong motion data recorded by the surface–downhole network. In addition, both the P-wave and S-wave velocity profiles measured by the suspension PS-logging systems at 12 stations were compiled in this study to calculate the average S-wave velocity of the top 30-m layer (Vs30) and the average S-wave velocity for the whole borehole depth (VsZ).

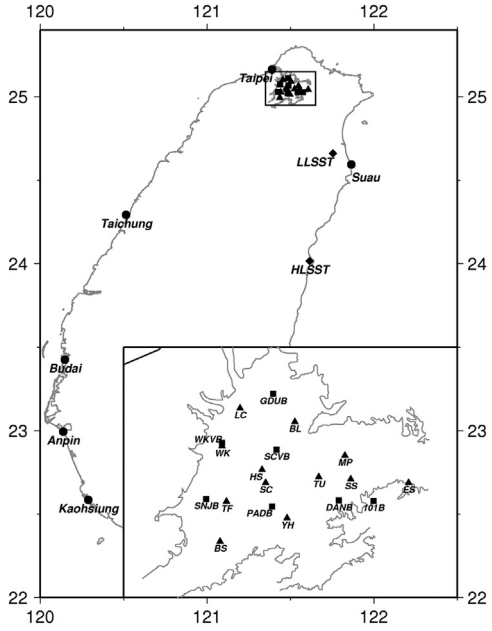

Fig. 1. Locations of downhole seismic arrays in Taiwan. The lower right map show the distributions inside the Taipei Basin. The circles are Harbor downhole arrays; the diamonds are LSST downhole arrays; the triangles are strong motion downhole arrays in the Taipei Basin; the squares are broadband downhole arrays in the Taipei Basin.

2. Data acquisition and processing

In this section, we briefly introduce the national surface–downhole network, which is under construction by the CWB, and the selected 15 stations that had already recorded a number of data sets for the analysis of the local site effects. In this study, the accelerations were processed as described below before use. In addition, we employed data from 26 stations that recorded four large events to generate intensity distribution maps for both the surface and downhole conditions. The data were also used to examine the difference between the estimated local surface and downhole magnitudes.

2.1. Surface–downhole network

A network of surface–downhole stations is under construction by the CWB to improve earthquake monitoring, earthquake location determination, and early warning capabilities. The real-time digital data recorded by all stations in the network are delivered to the Seismological Center of the CWB. The 15 stations shown in Fig. 2 were selected in this study to evaluate site effects. Each station includes a pair of force balance accelerometers, one at the surface and another at the borehole, and a broadband velocity seismometer. Fig. 3(a) illustrates the equipment configuration at the stations. A 24-bit data recorder is placed at the surface to receive seismic data from three sensors at a sampling rate of 100 Hz. The layout of the network is similar to that of the KiK-net of Japan. The strong motion data derived from this network are suitable for studying site effects in Taiwan, because this network provides accelerations both at the surface and bedrock.

Each observation borehole is drilled into engineering bedrock (S-wave velocity of the engineering bedrocks may vary from 300 m/s to larger than 1100 m/s), reaching an average depth of 300 m, to enable the accelerometer pairs to record ground motions both at the bedrock

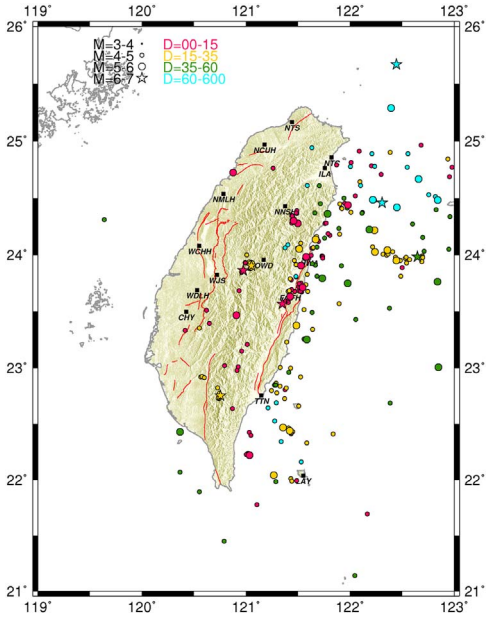

Fig. 2. Locations of the 15 selected surface–downhole stations, and the distribution of epicenters of the selected earthquakes ($M_L \geq 4$). The black squares denote the locations of the stations together with the station codes. Magnitudes are indicated by circles of different sizes and stars. The symbols are filled by colors to express the ranges of the focal depths (For interpretation of the references to color in this figure legend, the reader is referred to the web version of this article.)

and surface. Of the 15 stations used in this study, the deepest observation borehole is located at the CHY station (397-m deep), whereas the shallowest borehole is located at the ILA station (177-m deep). The downhole broadband seismometers are installed at the bottom of the observation boreholes to reduce artificial noise from the surface; therefore, high-quality data can be obtained, even from a local microearthquake.

This study used only acceleration data to analyze site effects. Fig. 3(b) shows a data set of accelerations recorded at the CHY station

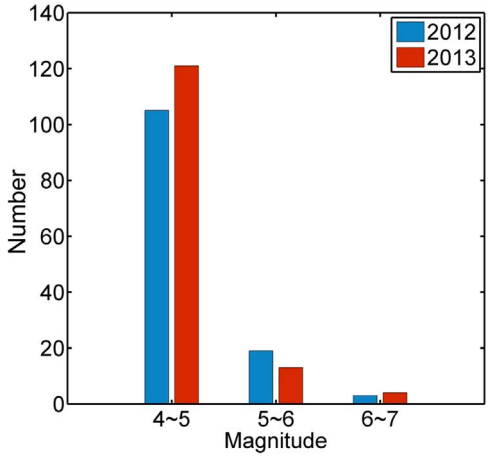

Fig. 4. Distribution of earthquakes by magnitude over the 2 years of interest. The earthquake frequencies for the three magnitude bins from left to right are 105, 19, and 3 in 2012 and 121, 13, and 4 in 2013.

as an example. The accelerations at the surface (left) were higher than those in the borehole (right), owing to the site amplifications.

2.2. Data processing

We acquired seismic data for earthquakes with local magnitudes (M_L) ≥ 4 that occurred in 2012 and 2013. The distribution of their epicenters is shown in Fig. 2. The earthquake magnitudes are indicated by circles of different sizes, and stars are used to represent earthquakes with a magnitude ranging from 6 to 7. In Taiwan, no events with a magnitude > 7 have been recorded in recent years. The aforementioned symbols are filled by colors to express the ranges of focal depths, as shown in the legend of Fig. 2. However, the real-time digital data streams can become unstable during strong shaking, and seismic data packets are occasionally lost. A total of 265 events were included in the analysis. Fig. 4 illustrates the distribution of the included events by magnitude and year.

The directions of the horizontal components of the downhole

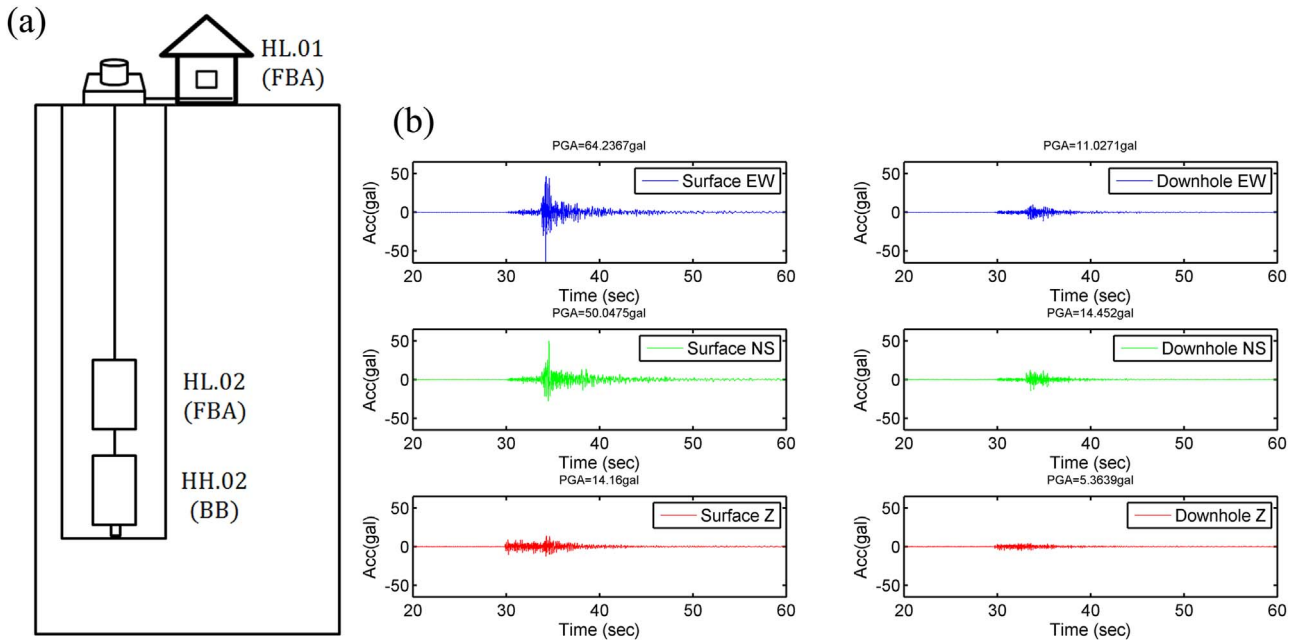

Fig. 3. (a) Illustration of the instrumentation configuration at a surface–downhole station. FBA (HL) indicates a force balance accelerometer, and BB (HH) indicates a broadband sensor. The numbers 01 and 02 indicate the locations at the surface and downhole, respectively. (b) Accelerograms of the FBA instruments at the surface (left) and downhole (right) are the same scale.

Table 1
Basic information of the stations used in the study.

Station Code	Lon.	Lat.	Elevations	Angle	Vs30 (m/s)	VsZ (m/s)	Site class
CHY	E 120.4325	N 23.4963	27 & −370	337	479	593	C
EGFH	E 121.4274	N 23.6688	132 & −163	0	NA	NA	NA
HWA	E 121.6135	N 23.9751	16 & −273	144	301	310	D
ILA	E 121.7563	N 24.7638	7 & −170	0	233	295	D
LAY	E 121.5581	N 22.0373	324 & 128	0	NA	NA	NA
NCUH	E 121.1849	N 24.9679	153 & −143	212	368	500	C
NMLH	E 120.7910	N 24.5372	201 & −95	0	498	595	C
NNSH	E 121.3829	N 24.4284	1106 & 813	88	538	575	C
NTC	E 121.8297	N 24.8544	4 & −288	0	400	449	C
NTS	E 121.4492	N 25.1644	16 & −276	0	276	400	D
OWD	E 121.1759	N 23.9545	1263 & 973	0	NA	NA	NA
TTN	E 121.1549	N 22.7524	9 & −287	40	506	603	C
WCHH	E 120.5583	N 24.0795	34 & −262	185	500	615	C
WDLH	E 120.5381	N 23.6888	69 & −227	0	358	376	D
WJS	E 120.7279	N 23.8219	175 & −117	247	679	974	C

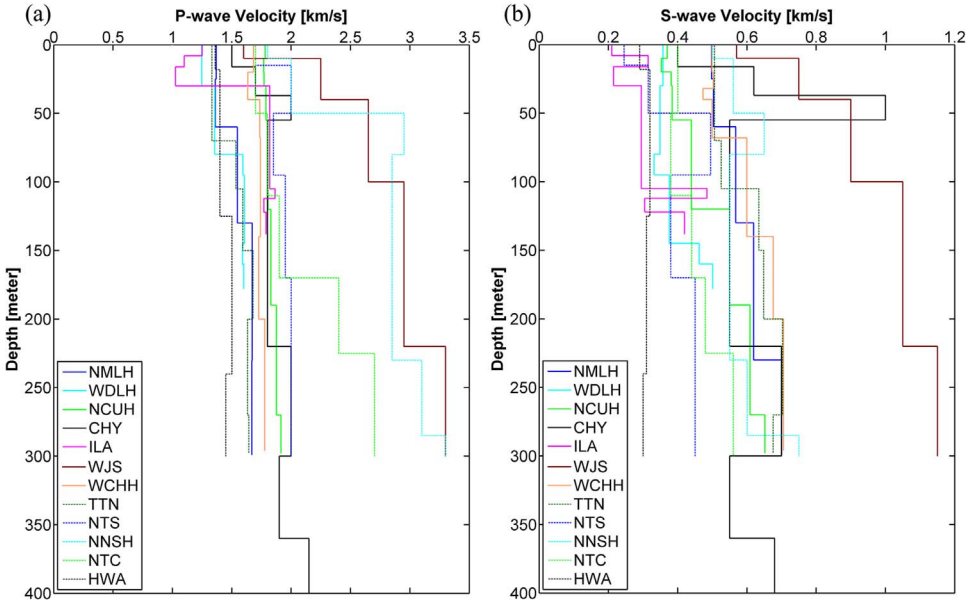

Fig. 5. Compiled (a) P-wave velocity profiles and (b) S-wave velocity profiles at 12 stations. The velocities were measured using the PS-logging method before the installation of the sensors.

accelerometers have an offset from north at several stations; thus, we had to rotate the angle for these horizontal recordings. Finally, a baseline correction was performed for all recordings by removing the mean value of the first 3 s. The basic information of the 15 stations listed in Table 1 includes the coordinates, elevations of the surface and downhole accelerometers, offset angles of the downhole accelerometers, Vs30, VsZ, and the site classes. The Vs30 values were obtained from the compiled results of PS-logging measurements. The compiled velocity profiles are plotted in Fig. 5.

According to the results, all 15 stations belong to classes C and D on the basis of the Vs30 criterion of the National Earthquake Hazard Reduction Program [35]. Wang *et al.* [33] calculated the average P-wave and S-wave velocities for the 28 stations included in their study. They compared their calculated average S-wave velocities with the compiled results, and the comparison showed that the results were comparable at most stations, except for the NNSH station, at which very limited data were acquired.

3. Methodology

To evaluate seismic site effects, this study analyzed PGAs and empirical transfer functions in the time and frequency domains by using the strong motion data recorded by the surface–downhole stations. In addition, we assessed the differences in the estimated magnitude by using the surface and downhole data.

3.1. Site amplification of PGA

We used the horizontal accelerations recorded by the surface–downhole stations to calculate the PGA amplification factor of seismic waves propagating from the bedrock to the surface. A horizontal PGA is calculated as the geometric mean of the north–south and east–west components using

$$PGA_H = \sqrt{PGA_{NS} \times PGA_{EW}} \quad (1)$$

where PGA_H is the horizontal PGA, and PGA_{NS} and PGA_{EW} are the PGAs of the north–south and east–west directions, respectively.

The PGA amplification factor at a surface–downhole station is subsequently calculated as

$$AMP = PGA_S/PGA_D \quad (2)$$

where AMP is the amplification factor, PGA_S is the PGA of surface acceleration, and PGA_D is the PGA of downhole acceleration. For each station, an amplification factor was calculated for every single event by using Eq. (2); subsequently, an average amplification factor and standard deviation were derived for that station.

Under other conditions, the PGA at the surface can be regarded as a function of the downhole PGA for each station. We adopted a power

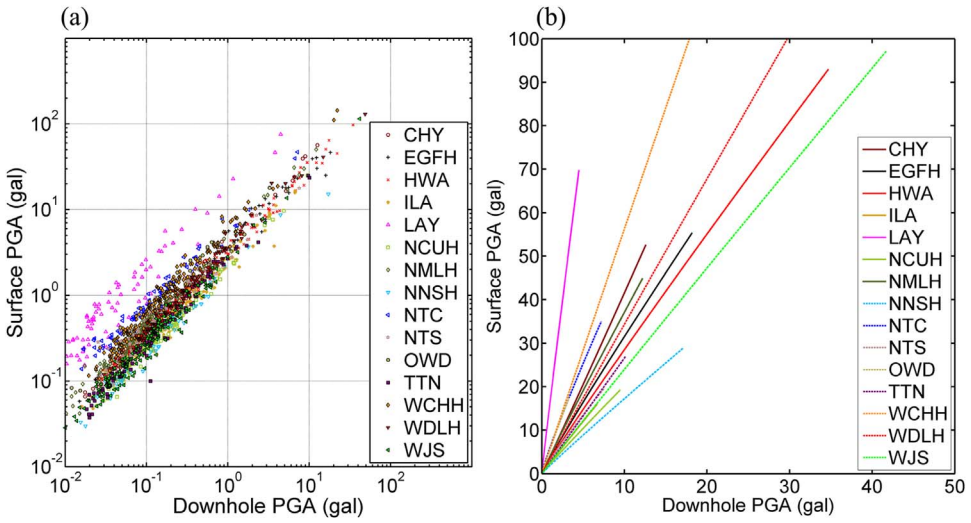

Fig. 6. (a) Distribution of PGAs downhole (*x*-axis) and at the surface (*y*-axis). (b) The power law relationships between the downhole and surface PGAs at each station, as listed in Table 2.

Table 2
PGA amplifications at the stations from downhole to the surface as a factor and a power law relationship.

Station code	AMP_{avg}	AMP_{std}	Relationship
CHY	3.88	0.58	$PGA_S = 3.97 \times PGA_D^{1.02}$
EGFH	3.93	0.87	$PGA_S = 3.62 \times PGA_D^{0.94}$
HWA	3.41	0.58	$PGA_S = 3.20 \times PGA_D^{0.95}$
ILA	2.59	0.47	$PGA_S = 2.48 \times PGA_D^{0.98}$
LAY	20.01	6.93	$PGA_S = 16.47 \times PGA_D^{0.96}$
NCUH	2.47	0.57	$PGA_S = 2.22 \times PGA_D^{0.96}$
NMLH	4.48	0.83	$PGA_S = 4.07 \times PGA_D^{0.96}$
NNSH	2.10	0.40	$PGA_S = 1.89 \times PGA_D^{0.96}$
NTC	7.81	1.95	$PGA_S = 6.04 \times PGA_D^{0.89}$
NTS	3.96	1.32	$PGA_S = 3.18 \times PGA_D^{0.90}$
OWD	6.45	1.30	$PGA_S = 5.68 \times PGA_D^{0.94}$
TTN	2.67	0.46	$PGA_S = 2.66 \times PGA_D^{1.00}$
WCHH	5.95	1.19	$PGA_S = 5.76 \times PGA_D^{0.99}$
WDLH	3.71	0.54	$PGA_S = 3.60 \times PGA_D^{0.98}$
WJS	2.69	0.55	$PGA_S = 2.51 \times PGA_D^{0.98}$

law equation to develop a relationship to understand how amplification varies with increasing PGA.

$$PGA_S = a \times PGA_D{}^b \quad (3)$$

where coefficients a and b are evaluated during the regression. The exponential coefficient b of the equation is usually smaller than 1, indicating the reduced PGA amplifications as PGA increased, that is, the behavior of ground motion nonlinearity during strong shaking. An average amplification factor with a standard deviation and the power law amplification relationship for PGA were derived in this study to understand the site effect on PGA at the 15 stations.

3.2. Empirical transfer function

In addition to estimating PGA amplification in the time domain, this study analyzed the empirical transfer function to understand the entire site effect at different frequencies. The Fourier spectral ratio between a soil station and a rock station is typically regarded as an empirical transfer function that is representative of the site effect [3]. The frequency range between 0.1 and 20 Hz is considered for the empirical transfer functions in this study. However, the soil and rock stations used must be very close to each other; thus, an adequate rock site is usually very difficult to be identified. A seismic time history is a convolution of the source, path, and site effects and can be further considered as a product of the three effects in the frequency domain.

$$A(f) = E(f) \times P(f) \times S(f), \quad (4)$$

where A(f) is the spectrum of a seismic time history, and E(f), P(f), and S(f) are the source, path, and site effects, respectively, in the frequency domain. When the seismic data of an earthquake are used to analyze the site effect, the hypocentral distance from a soil site to a reference rock site is approximated; subsequently, the source and path effect can be eliminated using the following equation to extract the transfer function of the site effect ($S_T(f)$).

$$S_T(f) = A_S(f)/A_R(f) = S_S(f)/S_R(f), \quad (5)$$

where A_S and A_R are the spectra of the soil site and the rock site, respectively, and S_S and S_R are the site effects at the soil site and the rock site, respectively.

The HVSR method is an alternative approach for estimating the site effect, and is a single-station method that was first proposed by Nakamura [4] on the basis of examinations of both earthquake and microtremor data.

$$S_{TT}(f) = S_{HS}(f)/S_{VS}(f) \quad (6)$$

where S_{TT} is the spectral ratio of the horizontal (S_{HS}) and vertical spectra (S_{VS}) at the surface. Nakamura [4] proposed that the HVSR approach could eliminate the influence of the Rayleigh waves that are usually caused by near-surface soil layers to yield a result comparable with that of the two-station method.

A reference rock site is not required in this method; thus, it has become extensively applied, particularly for microtremor analysis. Lermo and Chávez-Garcia [7] also confirmed that this method can be applied to strong motion data. A horizontal spectrum used with the two-station and single-station methods, as shown in Eqs. (5) and (6), is a quadratic mean of the Fourier spectra for the north–south and east–west seismic data in this study.

3.3. Estimation of local magnitude (M_L)

Local magnitude, that is, the Richter magnitude scale [36], is the official scale used by the CWB in Taiwan. The local magnitude is determined by the peak amplitude of the seismic waves recorded using a Wood–Anderson seismometer. The seismic amplitudes recorded by the surface and downhole accelerometers at a station are considerably different, owing to the site effect caused by the soft layers between the surface and bedrock; thus, this difference results in a divergence of the calculated local magnitude. In Taiwan, the local magnitude is calculated using three equations proposed by Shin [37].

$$\log A_0 = -0.00716 \times R - \log_{10}(R) - 0.39 \quad (7)$$

$$\log A_0 = -0.00261 \times R - 0.83 \times \log_{10}(R) - 1.07 \quad (8)$$

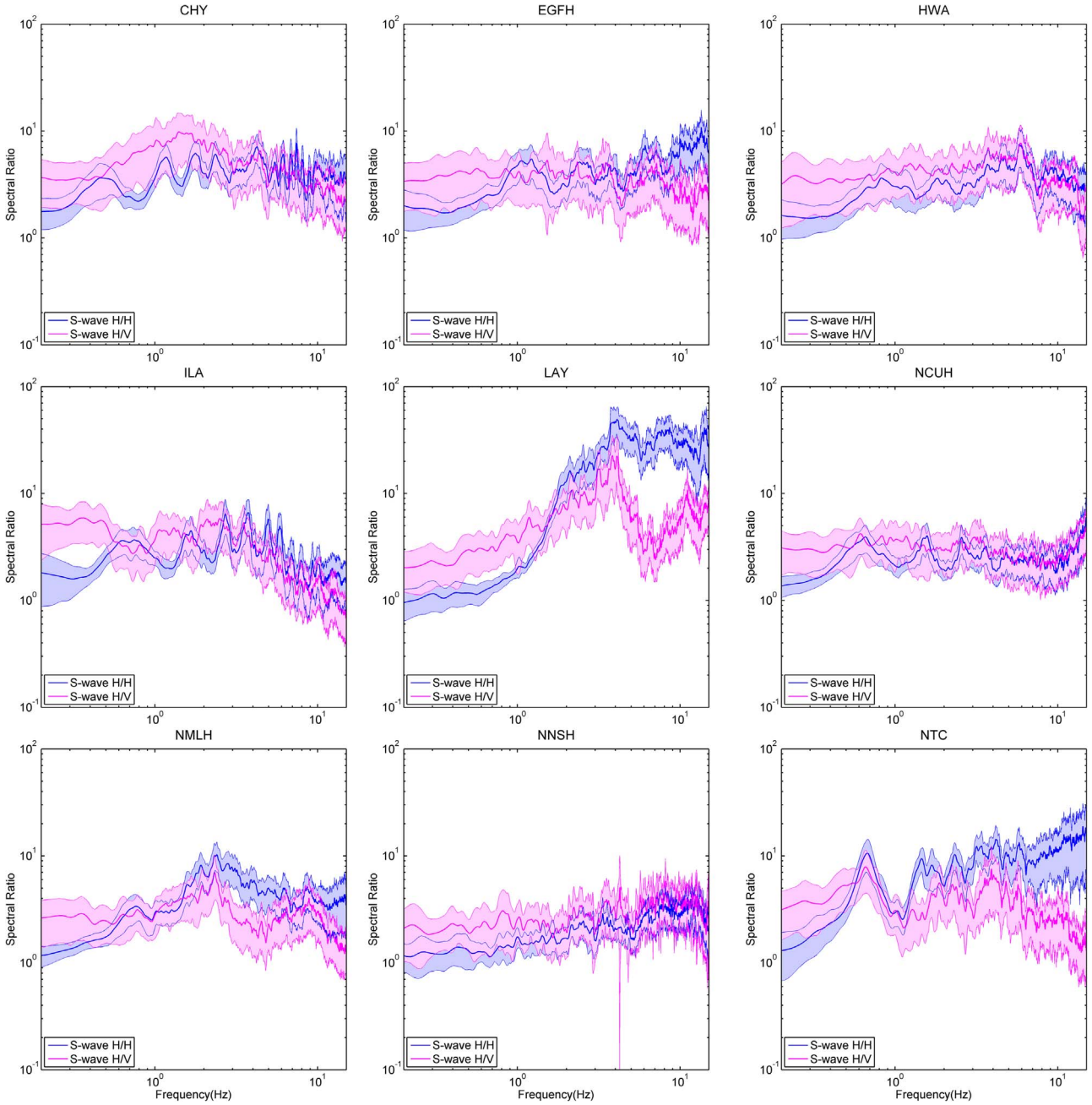

Fig. 7. HHSR (blue) and HVSR (red) ranges within 1 standard deviation at CHY, EGFH, HWA, ILA, LAY, NCUH, NMLH, NNSH, and NTC. (For interpretation of the references to color in this figure legend, the reader is referred to the web version of this article.)

$$\log A_0 = -0.00326 \times R - 0.83 \times \log_{10}(R) - 1.01 \quad (9)$$

where A_0 is the peak amplitude of the reference earthquake recorded using a Wood–Anderson seismometer, and R is the epicentral distance for an earthquake. Eqs. (7) and (8) are used for shallow earthquakes with a focal depth of ≤ 35 km; Eq. (7) is used for near events with epicentral distances of ≤ 80 km, whereas Eq. (8) is used for far events with epicentral distances of > 80 km. Eq. (9) is used for moderate and deep earthquakes with a focal depth of > 35 km.

4. Site amplification and the effect on magnitude determination

The horizontal PGAs were calculated at both the surface and downhole for events at each station, and the distributions are shown in Fig. 6(a). The relationships shown in Fig. 6(b) were evaluated using Eq. (3). Under other conditions, the mean amplification factors and standard deviations at the stations were calculated using Eq. (2). PGA amplifications from the downhole bedrock to the surface for each station are provided in Table 2 as a factor and a power law relationship.

For the empirical transfer functions, both the two-station and single-station methods were adopted to evaluate the site amplifications at different frequencies. The two-station method derives the HHSR at the surface and downhole, whereas the single-station method derives the HVSR at the surface. To avoid nonlinearity during strong shaking, the S-wave portions of accelerations of PGAs smaller than 50 gal were used to calculate the spectral ratios. The average two-station and single-station spectral ratios were plotted in the same graph by using a blue curve and a red curve, respectively, together with the spectral ratios at + 1 and − 1 standard deviations. The results for the stations are shown in Figs. 7 and 8.

Seven earthquakes with local magnitudes > 6 occurred in Taiwan

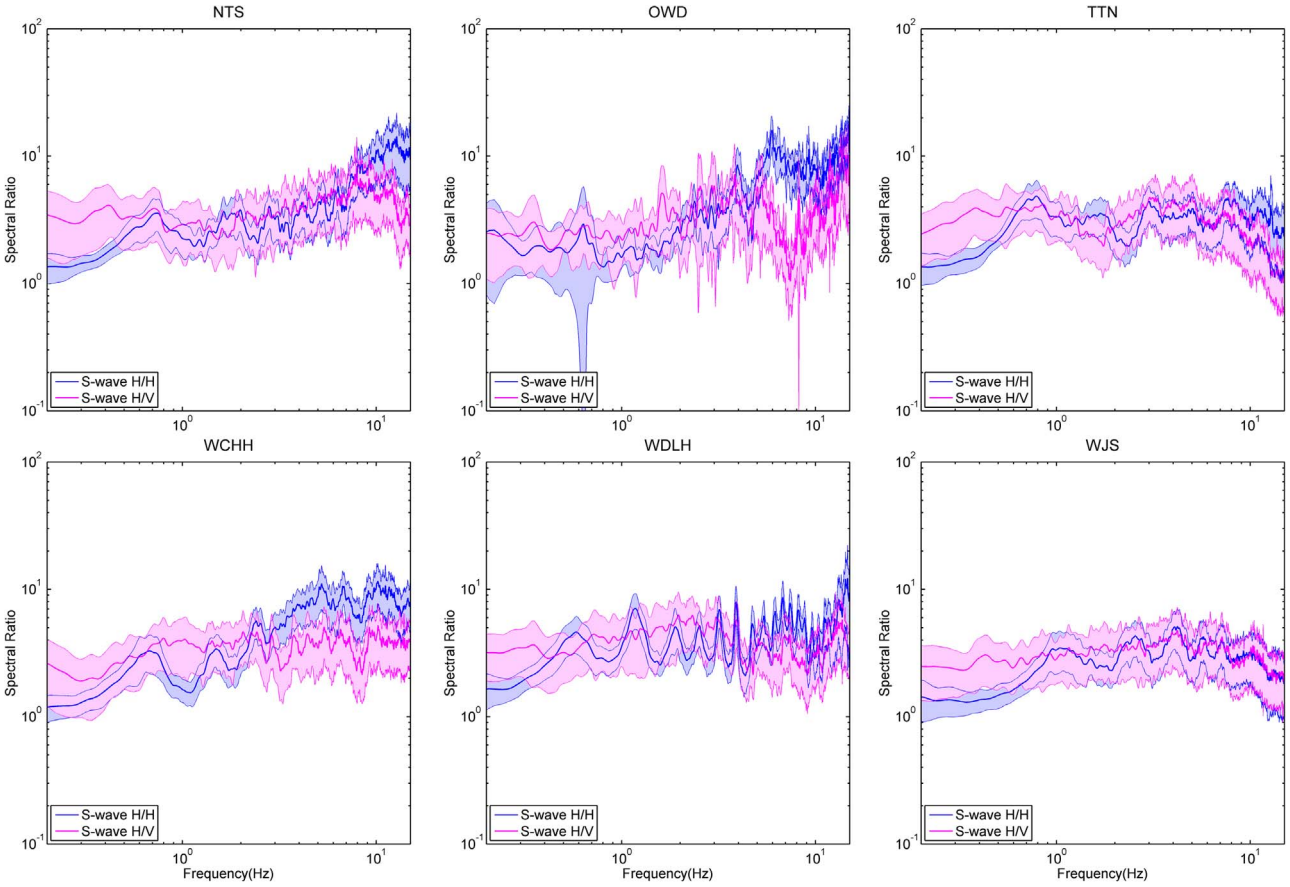

Fig. 8. HHSR (blue) and HVSR (red) ranges within 1 standard deviation at NTS, OWD, TTN, WCHH, WDLH, and WJS. (For interpretation of the references to color in this figure legend, the reader is referred to the web version of this article.)

during 2012 and 2013. Four of these were inland crustal earthquakes that were comprehensively recorded by the surface–downhole network. They were the Wutai earthquake (M_L = 6.4), which occurred on February 26, 2012; the Nantou earthquake (M_L = 6.2), on March 27, 2013; another Nantou earthquake (M_L = 6.5), on June 6, 2013; and the Hualien earthquake (M_L = 6.4), on October 31, 2013. The four earthquakes were felt throughout Taiwan and thus provide an opportunity to identify the divergence of strong motions with and without site effects at the surface and downhole locations of the network. Intensity distribution maps for the four large earthquakes were generated using data from 26 stations in the surface–downhole network and are illustrated in Fig. 9. The stations in each intensity distribution map are denoted by a black square, and the corresponding intensity according to the criterion of the CWB is shown below. In Taiwan, the official intensity grades used by the CWB is determined by PGA (Table 3). The legend of Fig. 8 shows the intensity grades from 0 (PGA < 0.8 gal) to 7 (PGA > 400 gal) in different colors.

This study used 15 stations with sufficient records to further analyze site effects in detail; however, all surface–downhole stations that recorded the four large earthquakes are illustrated in the intensity distribution maps. To assess the differences in the estimated M_L by using the surface and downhole data at each station, the same four large earthquakes were used again. Otherwise, we selected eight events for magnitudes of 5–6 (4 events) and 4–5 (4 events), respectively to check the differences in different magnitudes. The differences in the estimated M_L values from the surface and borehole at the 26 stations for the three magnitude intervals are presented in Table 4. The average difference at each station for magnitude larger than 6 is illustrated in Fig. 10. Magnitudes unavailable because of lost or abnormal accelerograms are marked as not available (NA) in Table 4.

5. Discussion

The results of the PGA amplification analysis shown in Fig. 6 and Table 2 indicate that the PGA amplification factors ranged from 2 at NNSH to 20 at LAY. However, the amplification factors at most stations ranged from 2 to 5. At several stations, a weak nonlinear correlation was observed by PGA amplifications between the downhole and surface as PGA increased. The amplification caused by the sedimentary layers resulted in an increase in the PGA at the surface, whereas nonlinearity reduced PGA amplification as PGA increased. Thus, the exponent of the regressed relationship in Table 2 was evidently smaller than 1 at several stations (e.g. HWA, NTC, and OWD). However, we do not further discuss this issue in detail because relative few recordings have high PGA values.

The four large earthquakes are shown as examples in Fig. 9. On average, the intensities at the surface were usually one grade higher than those downhole. This amplification is significant because it is caused by very thin unconsolidated sediments (less than 400 m) in comparison with the focal depths (10–20 km). The observations indicated that the shaking intensity was attenuated to one grade over a horizontal distance of approximately 40 km from the source (Fig. 9). By contrast, the site amplifications showed dramatic increases in intensity along the vertical direction owing to the inhomogeneous properties of the layered materials in this direction.

Site amplification is ground motion at the surface relative to that at a uniform bedrock [18]. However, the Vs of the bedrock in the boreholes vary from 300 m/s to more than 1100 m/s (Fig. 5(b)). The nonuniform bedrock causes irregular amplifications; thus, the derived site amplification factors are not suitable to correlate with Vs30.

The spectral ratios obtained using the HHSR and HVSR methods showed comparable patterns and similar dominant frequencies and

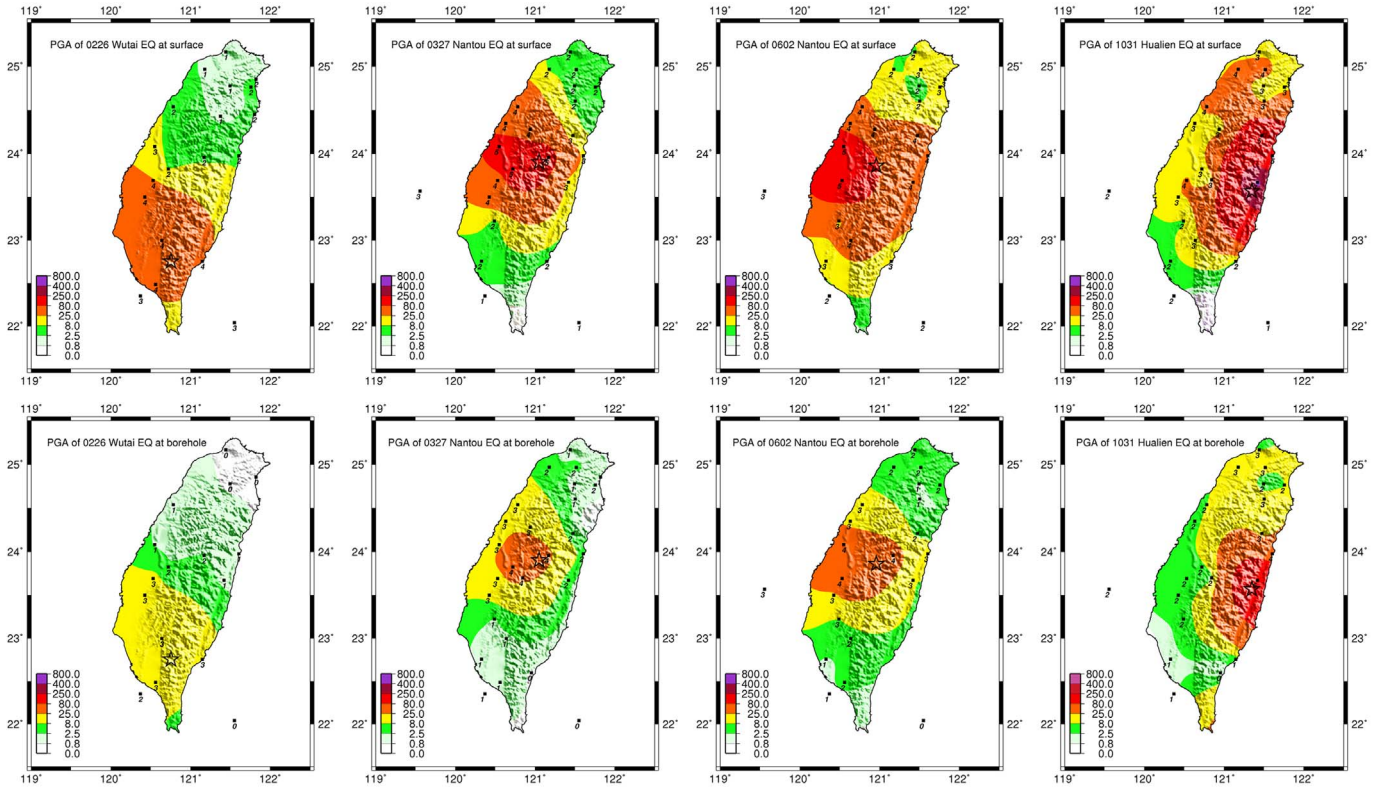

Fig. 9. Intensity distribution maps at the surface (above) and downhole (below) of the Wutai earthquake occurring on February 25, 2012; the first Nantou earthquake occurring on March 27, 2013; the second Nantou earthquake occurring on June 2, 2013; the Hualien earthquake occurring on October 31, 2013, are illustrated from left to right, respectively. The stations used are denoted with a black square and with the intensity shown below. The legend shows the intensity grades in different colors. (For interpretation of the references to color in this figure legend, the reader is referred to the web version of this article.)

Table 3
The CWB's intensity and the corresponding PGA used in Taiwan.

CWB intensity	PGA (gal)
0	< 0.8
I	0.8–2.5
II	2.5– 8
III	8–25
IV	25–80
V	80–250
VI	250–400
VII	> 400

amplifications. However, some differences were still observed in the results. For example, the HHSR method not only indicates a clear peak at the dominant frequency but also shows clear peaks at higher resonant frequencies. The spectral ratios are helpful for understanding the site amplifications at these frequencies. For example, station LAY showed a much higher PGA amplification factor than the other stations. The HHSR at LAY showed extremely high amplification of approximately 30 at frequencies higher than 3.5 Hz, and this sizeable amplification at the high frequency is the reason for PGA amplification. The average HHSR value at frequencies of 5–10 Hz was calculated at each station, and Fig. 11(a) shows the distribution of the PGA amplification factors (Table 2) and the regressed linear equation. The high correlation coefficient of 0.99 indicated that HHSR at the specific frequency was highly correlated with PGA amplifications.

The spectral ratios at the dominant frequencies of the HHSR and HVSR methods were comparable at most stations in this study. Exceptions in the spectral ratios (those outside the range of 1 standard deviation) were observed at LAY, NTC, and OWD. The HHSR was higher than the HVSR at the dominant frequencies of 4 Hz and 0.7 Hz at LAY and NMLH, respectively. Compared with a horizontal spectrum at the borehole, a vertical spectrum at the surface had lower values at low frequencies but higher values at high frequencies. Contribution of P-wave in vertical component and conversion of P-wave and SV-wave at the boundaries of the layers above the base rock, which are sensitive to the presence of local heterogeneities and a complex 2D or 3D subsurface geometry, are significant at high frequencies for HVSR. Therefore, the HVSRs were higher at low frequencies and lower at high frequencies. This observation is because a vertical component record usually contains more high-frequency seismic waves but less low-frequency seismic waves in comparison with a horizontal record. The differences in the frequency content of the horizontal and vertical spectra lead to differences in the resultant HHSR and HVSR.

This study further introduced normalized root-mean-square deviation (NRMSD) as an index to quantify the discrepancy between HHSR and HVSR. The NRMSD is defined as

$$\mathrm{NRMSD} = \left(\sum_{i=f1}^{f2} (\mathrm{HHSR_i} - \mathrm{HVSR_i})^2/n\right)^{1/2} / \left(\sum_{i=f1}^{f2} \mathrm{HHSR_i}/n\right) \quad (10)$$

where *f1* and *f2* are the frequency range used for the quantification, and *n* is the number of frequency points. The whole frequency range of 0.1–20 Hz was used to calculate the NRMSD. In addition, we selected a medium frequency range of 0.5–10 Hz for an alternative calculation. The average NRMSD for the whole frequency range at the 15 selected stations was found to be 0.50, whereas the NRMSD reduced to 0.42 for the medium frequency. Moreover, the NRMSD of the HHSR and itself +1 or −1 standard deviation for the whole frequency range at the 15 stations was 0.46. The result indicates that the HVSR can be used instead of the HHSR, because it is usually difficult to obtain, particularly for the medium frequency range, which is important for engineering applications.

Table 4
Estimated local magnitudes at the surface (SF) and downhole (DH) at stations for the four large earthquakes of M_L > 6, 5–6, and 4–5. Four earthquakes are used for each magnitude range. The last row shows the average difference between the estimated magnitudes at the surface and downhole at each station.

Station code	M > 6		5 < M < 6		4 < M < 5		Average difference		
	SF	DH	SF	DH	SF	DH	> 6	5–6	4–5
CHY	6.71	6.18	5.67	5.09	4.56	3.98	0.53	0.57	0.59
EGFH	6.26	5.70	5.32	4.79	4.17	3.55	0.56	0.53	0.63
HWA	6.47	6.14	5.46	4.97	4.55	4.04	0.33	0.48	0.51
ILA	6.69	6.26	5.65	5.24	4.80	4.30	0.42	0.42	0.51
LAY	5.92	5.41	6.92	5.47	NA	NA	0.51	1.45	NA
NCUH	6.70	6.39	5.72	5.34	4.31	3.93	0.30	0.39	0.39
NDT	6.20	5.94	5.38	5.05	4.02	3.65	0.26	0.34	0.37
NHDH	6.64	6.31	5.75	5.32	4.58	4.07	0.33	0.43	0.52
NMLH	6.78	6.28	5.80	5.30	4.68	4.05	0.50	0.50	0.63
NTC	6.60	5.90	5.66	4.99	4.54	3.70	0.70	0.67	0.84
NTS	6.71	6.28	5.75	5.42	4.57	4.18	0.43	0.34	0.39
NWL	6.01	5.91	5.17	5.02	NA	NA	0.10	0.15	NA
OWD	6.04	5.83	5.31	5.07	NA	NA	0.21	0.25	NA
PNG	6.53	6.34	5.17	4.91	NA	NA	0.20	0.26	NA
SLG	6.43	5.90	4.81	4.64	3.76	3.42	0.54	0.17	0.35
SNJ	6.58	6.00	5.55	4.76	4.07	3.21	0.59	0.78	0.86
SNS	6.31	6.03	5.27	4.87	3.95	3.57	0.27	0.40	0.38
SSP	6.10	5.98	5.07	4.62	NA	NA	0.12	0.45	NA
TTN	6.13	5.77	5.45	4.92	4.19	3.81	0.36	0.53	0.39
WCHH	6.56	6.11	5.55	5.22	4.57	4.07	0.45	0.33	0.50
WDJ	6.57	6.40	5.60	5.33	4.09	3.83	0.18	0.28	0.26
WDLH	6.81	6.34	5.61	5.09	4.59	4.05	0.47	0.51	0.54
WHP	6.40	6.17	5.52	5.07	4.12	3.63	0.23	0.45	0.49
WHY	5.87	5.63	5.04	4.58	NA	NA	0.24	0.46	NA
WJS	6.36	6.03	5.42	4.99	4.21	3.77	0.33	0.44	0.44
WLCH	6.33	6.09	5.13	4.81	4.32	4.01	0.24	0.32	0.31

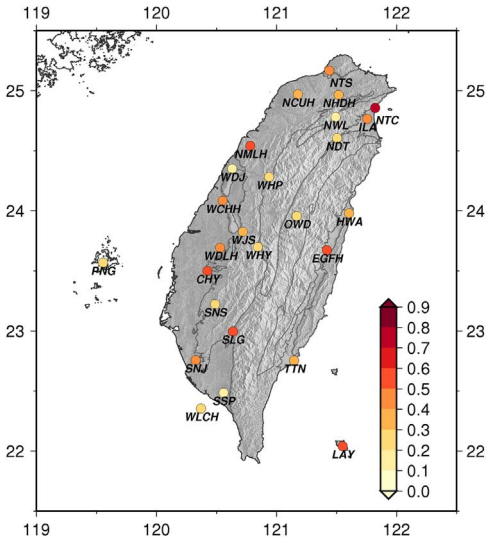

Fig. 10. Differences in estimated local magnitudes between the surface and downhole at 26 stations.

Fig. 9 shows the intensity distribution maps of strong motions at the surface and downhole, which can be considered to be maps of strong motions with and without site effects, respectively. The intensity distribution map at the surface with site amplification showed higher intensities than that in the borehole without site amplification. The same four events with magnitudes > 6 were used to identify differences between estimated local magnitudes caused by the site effect. The local magnitude was derived using an instrument (Wood–Anderson type seismometer) with a natural period of 0.8 s (1.25 Hz); thus, the estimated magnitude can reflect the seismic response at an important frequency for engineering applications.

As shown in Table 4, the estimated M_L for the Wutai earthquake (0226) was 6.33 at the surface and 5.91 downhole. For the first Nantou earthquake (0327), the estimated M_L was 6.32 at the surface and 5.93 downhole. For the second Nantou earthquake (0602), the estimated M_L was 6.54 at the surface and 6.15 downhole. For the Hualien earthquake, the estimated M_L was 6.58 at the surface and 6.27 downhole. The differences for each event were 0.42, 0.39, 0.39, and 0.31, respectively; therefore, the magnitude derived using the surface data was higher by 0.36 on average than that derived using the downhole data (Table 4). The differences in the estimated magnitudes at each station are plotted in Fig. 10. The finding indicated that the stations located in plains and basins showed larger differences than those in mountainous areas. However, large differences in magnitude were also found for stations located near the edges of basins and in piedmonts between plains and mountains. For example, the smaller differences with values less than 0.25 were found at NWL, OWD, PNG, SNS, SSP, WDJ, WHP, WHY, and WLCH. Except for the PNG and WLCH sites located on Penghu Island and Liqiu Island, respectively, only SSP and WDJ are not located in a mountainous area. The difference at SSP was calculated from only one large event. The WDJ station is located near a terrace, and a small magnitude difference of 0.18 on average was found at this station. The larger magnitude differences were 0.7, 0.56, 0.53, and 0.54 at NTC, EGFH, CHY, and SLG, respectively. The station LAY, which showed the highest PGA amplification, had a difference of 0.51 for the estimated magnitudes, as revealed using the surface and borehole records. For the events of magnitudes 4–5 and 5–6, the magnitude differences are larger than that of magnitude > 6 at most stations as shown in Table 4. The magnitude differences at surface and downhole are 0.49 and 0.46 for magnitudes 4–5 and 5–6, respectively.

The differences in magnitude > 6 could also be approximated from the HHSR at 1.1–1.7 Hz using a grid search approach, as shown in Fig. 11(b). The R of 0.89 demonstrated that HHSR at the specific frequencies was proportional to the magnitude difference. This result indicates that extreme seismic amplifications at the important frequencies of 1.1–1.7 Hz may occur at sites where impedance may exist between soft sediments and hard bedrock. This result also reveals that the local magnitudes estimated using the downhole recordings may have to be corrected to avoid underestimating the magnitudes. Without the magnitude correction, an inconsistency may be observed in the earthquake catalog; therefore, the annual seismicity and seismic hazard analysis may be affected.

6. Conclusions

Recently, the CWB of Taiwan has been constructing a national surface–downhole monitoring network. The strong motions recorded by the network facilitate the study of site amplifications through comparison of the surface and borehole data. The amplification factors at the selected 15 stations ranged from 2 at NNSH to 20 at LAY. However, the amplification factors at most stations ranged from 2 to 5 (Table 2). Under other conditions, the PGA at the surface was considered a function of the downhole PGA, and the relationships were also obtained (Table 2). The exponents of the regressed relationships were evidently smaller than 1 at several stations, indicating that soil nonlinearity reduced PGA amplifications as PGA increased.

Empirical transfer functions calculated using the HHSR and HVSR were also derived at the 15 stations (Figs. 7 and 8), representing amplifications at different frequencies. Therefore, PGA amplifications and differences in M_L were related to the HHSRs at 5–10 Hz and 1.1–1.7 Hz, respectively (Fig. 11). The R between HHSRs and PGA amplifications and M_L differences were 0.99 and 0.89, revealing very strong and strong correlations, respectively. Furthermore, we introduced the NRMSD to quantify the discrepancy between HHSR and HVSR at the 15 stations. The average NRMSD of the 15 stations was 0.50, whereas it reduced to 0.42 for the medium frequency of 0.5–10 Hz. For a comparison, the NRMSD of the HHSR and itself + 1 or − 1 standard deviation at the 15 stations was 0.46. Although the HHSRs usually showed

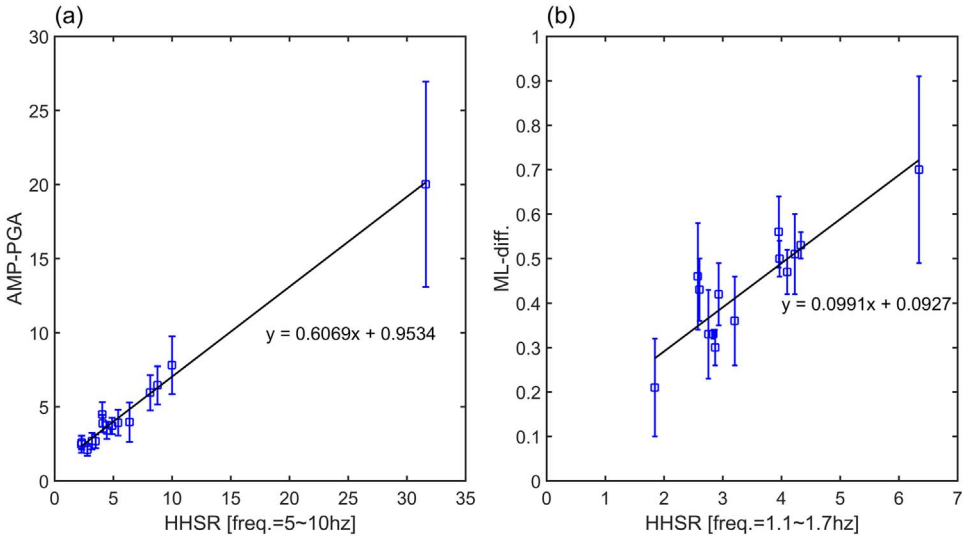

Fig. 11. (a) Distribution and correlation of PGA amplification with plus and minus one standard deviation and the corresponding HHSR at the frequency of 5–10 Hz. (b) Distribution and correlation of local magnitude difference (between surface and borehole) with plus and minus one standard deviation and the corresponding HHSR at the frequency of 1.1–1.7 Hz.

clearer peaks at resonant frequencies than the HVSRs, the small discrepancy suggests HVSR can be used instead of the HHSR, because the HHSR is usually difficult to obtain, particularly for the medium frequency range, which is important for engineering applications.

This study analyzed the M_L differences estimated using the data recorded by surface and downhole accelerometers at all the observed 26 stations (Table 4 and Fig. 10). The analysis used the recordings from twelve crustal earthquakes of $M_L > 6$, 5–6, and 4–5 with a resultant average difference of 0.36, 0.46, and 0.49, respectively. It is speculated that soil nonlinearity may reduce the amplitudes at stations suffered from strong shaking, so the magnitude difference is smaller in events of larger M_L. The stations located in plains and basins (e.g., NTS, NCUH, ILA, NMLH, HWA, TTN, SNJ, and SSP; 0.36 on average for $M_L > 6$) showed a larger difference than those in mountainous areas (e.g., NWAL, NDT, WHP, OWD, WHY, and SNS; 0.21 on average for $M_L > 6$) and offshore islands (e.g., PNG, WLCH, and LAY; 0.32 on average for $M_L > 6$). However, large differences in magnitude were found at stations located near the edges of basins or plains (e.g., NHDH, NTC, WJS, WDLH, CHY, WDJ, WCHH, SLG, and EGFH; 0.46 on average for $M_L > 6$). We learnt how the site effects affect the determination of local magnitude in different geological conditions. This result indicated that extreme seismic amplifications at the important frequencies of 1.1–1.7 Hz could occur at sites where impedance between soft sediments and hard bedrock may exist within borehole depths. An inconsistency may be observed in the earthquake catalog if the downhole data is directly adopted in magnitude estimation; therefore, the annual seismicity and seismic hazard analysis may be affected. The analysis revealed the necessity of developing new M_L equations particularly for the borehole data when the installation of surface–downhole network is finish.

Acknowledgments

We would like to thank the CWB of Taiwan for providing the seismic data of the surface–downhole network. This research was funded by the CWB under the projects MOTC-CWB-102-E-02 and MOTC-CWB-103-E-07. The Ministry of Science and Technology also supported this paper through grants MOST 105–2116-M-492-001 and MOST 105–2625-M-492-006.

References

[1] Milne J. Seismology. London: K. Paul, Trench, Trubner & co.; 1898.
[2] Wen KL, Lin CM, Chiang HJ, Kuo CH, Huang YC, Pu HC. Effect of surface geology on ground motions: the case of station TAP056 - Chutzuhu Site. Terr Atmos Ocean Sci 2008;19(5):451–62.
[3] Borcherdt RD. Effect of local geology on ground motion near San Francisco Bay. Bull Seismol Soc Am 1970;103(2A):1117–29.
[4] Nakamura Y. A method for dynamic characteristics estimation of subsurface using microtremor on the ground surface. Q Rep RTRI 1989;30(1):25–33.
[5] Borcherdt RD. Estimates of site-dependent response spectra for design. Earthq Spectra 1994;10(4):617–53.
[6] Borcherdt RD. Empirical evidence for acceleration-dependent amplification factors. Bull Seismol Soc Am 2002;92(2):761–82.
[7] Lermo J, Chávez-Garcia FJ. Site effect evaluation using spectral ratios with only one station. Bull Seismol Soc Am 1993;83(5):1574–94.
[8] Bonilla LF, Steidl JH, Lindley GT, Tumarkin AG, Archuleta RJ. Site amplification in the San Fernando Valley, California: variability of site-effect estimation using the S-wave, and H/V method. Bull Seismol Soc Am 1997;87:710–30.
[9] Kuo CH, Wen KL, Lin CM, Wen S, Huang JY. Investigating near surface S-wave velocity properties using ambient noise in Southwestern Taiwan. Terr Atmos Ocean Sci 2015;26(2):205–11.
[10] Liu KS, Shin TC, Tsai YB. A free-field strong motion network in Taiwan: TSMIP. Terr Atmos Ocean Sci 1999;10(2):377–96.
[11] Kuo CH, Wen KL, Hsieh HH, Chang TM, Lin CM, Chen CT. Evaluating empirical regression equations for Vs and estimating Vs30 in northeastern Taiwan. Soil Dyn Earthq Eng 2011;31(3):431–9.
[12] Kuo CH, Wen KL, Hsieh HH, Lin CM, Chang TM, Kuo KW. Site classification and Vs30 estimation of free-field TSMIP stations using the logging data of EGDT. Eng Geol 2012;129–130:68–75.
[13] Shin TC, Chang CH, Pu HC, Lin HW, Leu PL. The geophysical database management system in Taiwan. Terr Atmos Ocean Sci 2013;24(1):11–8.
[14] Wen KL, Peng HY. Site effect analysis in the Taipei basin: Results from TSMIP network data. Terr Atmos Ocean Sci 1998;9(4):691–704.
[15] Sokolov V, Wenzel F, Wen KL, Jean WY. On the influence of site conditions and earthquake magnitude on ground-motion within-earthquake correlation: analysis of PGA data from TSMIP (Taiwan) network. Bull Earthq Eng 2012;10(5):1401–29.
[16] Huang JY, Wen KL, Lin CM, Kuo CH, Chen CT, Chang SC. Site correction of high frequency strong ground motion simulation based on empirical transfer function. J Asian Earth Sci 2017;138:399–415.
[17] Ancheta TD, Darragh RB, Stewart JP, Seyhan E, Silva WJ, Chiou BSJ, Wooddell KE, Graves RW, Kottke AR, Boore DM, Kishida T, Donahue JL. NGA-West2 database. Earthq Spectra 2014;30(3):989–1005.
[18] Du W, Wang G. Intra-event spatial correlations for cumulative absolute velocity, arias intensity, and spectral accelerations based on region site conditions. Bull Seismol Soc Am 2013;103(2A):1117–29.
[19] CPA. Seismic Design Code and Commentary for Buildings. 2011 edn Construction and Planning Agency, Ministry of Interior Affair; 2011.
[20] Kuo CH, Cheng DS, Hsieh HH, Chang TM, Chiang HJ, Lin CM, Wen KL. Comparison of three different methods in investigating shallow shear wave velocity structures in Ilan, Taiwan. Soil Dyn Earthq Eng 2009;29(1):133–43.
[21] Kuo CH, Chen CT, Lin CM, Wen KL, Huang JY, Chang SC. S-Wave velocity structure and site effect parameters derived by microtremor arrays in the western plain of Taiwan. J Asian Earth Sci 2016;128:27–41.
[22] Lin CM, Wen KL, Lin CY, and Kuo CH, 2016. Receiver function analysis of strong-motion stations in Kaohsiung-Pingtung Area, Taiwan, EGU General Assembly 2016, Vienna, Austria, Apr. 17-22. (Abstract).
[23] Wen KL, Yeh YT, Huang WG. Effects of alluvial basin on strong ground motions. Bull Seismol Soc Am 1992;82(2):1124–33.
[24] Beresnev IA, Wen KL, Yeh YT. Source, path, and site effects on dominant frequency and spatial variation of strong ground motion recorded by SMART1 and SMART2 arrays in Taiwan. Earthq Eng Struct Dyn 1994;23(6):583–97.
[25] Wen KL, Beresnev IA, Yeh YT. Non-linear soil amplification inferred from downhole strong seismic motion data. Geophys Res Lett 1994;21(24):2625–8.

[26] Wen KL, Fei LY, Peng HY, Liu CC. Site effect analysis from the records of the Wuku downhole array. Terr Atmos Ocean Sci 1995;6(2):285–98.
[27] Huang WG, Huang BS, Wang JH, Chen KC, Wen KL, Tsao SH, Hsieh YC, Chen CH. Seismic observation in the Taipei metropolitan area using a downhole network. Terr Atmos Ocean Sci 2010;21(3):615–25.
[28] Chen KC, Lee FB, Chen JF, Hsieh MJ, Lai RI. Geotechnical monitoring and measures against liquefaction at harbor areas (3/3), MOTC-IOT-93-H1DA003. Taipei, Taiwan: Harbor and Marine Technology Center, Institute of Transportation, Ministry of Transportation and Communications; 2005. (In Chinese with English abstract).
[29] Aoi S, Kunugi T, Fujiwara H. Strong-motion seismograph network operated by NIED: K-NET and KiK-net. J Jpn Assoc Earthq Eng 2004;4(3):65–74.
[30] Kim B, Hashash YMA. Site response analysis using downhole array recordings during the March 2011 Tohoku-Oki earthquake and the effect of long-duration ground motions. Earthq Spectra 2013;29(S1):S37–54.
[31] Assimaki D, Li W, Steidl JH, Tsuda K. Site amplification and attenuation via downhole array seismogram inversion: a comparative study of the 2003 Miyagi-Oki aftershock sequence. Bull Seismol Soc Am 2008;98(1):301–30.
[32] Héloïse C, Bard PY, Rodriguez-Marek A. Site effect assessment using KiK-net data: part 1, a simple correction procedure for surface/downhole spectral ratios. Bull Earthq Eng 2012;10:421–48.
[33] Wang YJ, Ma KF, Wu SK, Hsu HJ, Hsiao WC. Near-surface attenuation and velocity structures in Taiwan from comparison of wellhead and borehole recordings. Terr Atmos Ocean Sci 2016;27(2):169–80.
[34] Lai TS, Mittal H, Chao WA, Wu YM. A study on kappa value in Taiwan using borehole seismic array. Bull Seismol Soc Am 2016;106(4):1509–17.
[35] BSSC. NEHRP recommended provisions for seismic regulations for new buildings and other structures. Washington, DC: Building Seismic Safety Council; 2001.
[36] Richter CF. An instrumental earthquake magnitude scale. Bull Seismol Soc Am 1935;25(1):1–32.
[37] Shin TC. The calculation of local magnitude from the simulated Wood-Anderson seismograms of the short-period seismograms in the Taiwan area. Terr Atmos Ocean Sci 1993;4(2):155–70.